Processes and mechanisms of the initial formation of the Siberian High during the autumn-to-winter transition

Lingying Chen[1,2] · Wen Chen[3,4] · Peng Hu[3,4] · Shangfeng Chen[1,2] · Xiadong An[5] · Tianjiao Ma[3,4] · Zhikai Wang[1,2]

Abstract

The Siberian High (SH), an important atmospheric system over Eurasia, exhibits notable seasonality—forming in autumn and peaking in the boreal winter. Many previous studies have revealed the characteristics of the SH in its peak phase; however, the SH formation process remains unclear. This study examined the climatological characteristics of SH formation with a cumulative sea-level-pressure series over the Siberian region based on observational data. First, the SH formation dates were objectively detected in both the climatology (October 1, 55th pentad) and individual years. Then, the thermodynamic processes around SH formation were investigated based on these formation dates. The results indicated that, in the lower troposphere, an anticyclonic circulation dominates over the Eurasian continent after SH formation. In the middle troposphere, an anomalous northeast–southwest-oriented ridge and trough appear over upstream of the SH and the coast of Northeast Asia, respectively. In the upper troposphere, the subtropical westerly jet, with its entrance located over the SH, intensifies and migrates southward, accompanying the amplification of its secondary circulation that features downward (upward) motion over Siberia (south of the Tibetan Plateau). The combined effects of the jet-associated circulation, negative vorticity advection and cold advection associated with the ridge and trough, and diabatic cooling contribute to high-level convergence and large-scale subsidence over the SH area, thereby resulting in SH formation. Further diagnosis reveals that dynamic processes play a more important role in SH formation than the thermal processes do.

1 Introduction

The Siberian High (SH), which resides over the Eurasian continent during the boreal winter, is a semi-permanent surface high that modulates the weather and climate over East Asia and remote regions (Ding and Krishnamurti 1987; Cohen et al. 2001; Jeong et al. 2011; Cheung et al. 2012; Tubi and Dayan 2013; Lü et al. 2019). The tight pressure gradient between the SH and the Aleutian low is essential for the prevalence of the East Asian winter monsoon (Chen et al. 2000; Takaya and Nakamura 2005a; Wang 2006; Chang and Lu 2012a; Liu and Zhu 2020; Dong et al. 2023). Cold air along with the monsoon flow induced by the enhanced SH can result in widespread cooling over East Asia (Keller et al. 2006; Liu and Zhu 2020) and lead to marked atmospheric convection over the tropical western North Pacific (Iqbal et al. 2013; Jia et al. 2014, 2015; Pang and Lu 2019; Ma et al. 2020, 2022). It has also been suggested that the SH may influence the El Niño–Southern Oscillation through the associated air–sea interaction and serve as a bridge for

✉ Wen Chen
chenwen-dq@ynu.edu.cn

1 Center for Monsoon System Research, Institute of Atmospheric Physics, Chinese Academy of Sciences, Beijing 100029, China

2 College of Earth and Planetary Sciences, University of Chinese Academy of Sciences, Beijing 100049, China

3 Yunnan Key Laboratory of Meteorological Disasters and Climate Resources in the Greater Mekong Subregion, Yunnan University, Kunming 650091, China

4 Department of Atmospheric Sciences, Yunnan University, Kunming 650500, China

5 Department of Marine Meteorology, College of Oceanic and Atmospheric Sciences, Ocean University of China, Qingdao 266100, China

linking the Arctic Oscillation and the East Asian climate (Gong et al. 2001; Wu and Wang 2002; Hasanean et al. 2013; Wu et al. 2015; Cheung and Zhou 2016; Fu et al. 2022). In addition, it is indicated that the SH plays an important role in contributing to winter warm anomalies over Barents-Kara Seas (Wu and Ding 2022). Essentially, the climate impacts of the SH are not only confined to local areas, but also to the entire Northern Hemisphere (Gong and Ho 2002; Chang and Lu 2012; Hasanean et al. 2013; Park and Ahn 2016; Riaz and Iqbal 2017; Park et al. 2021; Kim and Ahn 2023). Therefore, it is crucial for us to fully understand the SH as well as the mechanisms behind it.

Many previous studies have focused on the features of the SH in midwinter, especially its synoptic intensification (Ding 1990; Takaya and Nakamura 2005a; b; 2013; Zhou et al. 2009; Jeong et al. 2011; Hasanean et al. 2013; Pang and Lu 2019; Dai and Mu 2020; Dong et al. 2022; Kim and Ahn 2023). The results of these studies revealed that the sudden amplification of the SH is generally associated with cold-surge activity, which may cause severe impacts on East Asia, Southeast Asia, and the Maritime Continent. The amplification of the SH in midwinter has also been attributed to the combined effects of dynamic (i.e. mid–upper-level vorticity advection) and thermal (i.e. lower-level diabatic cooling and cold advection) processes (Ding and Krishnamurti 1987; Zhang et al. 1996; Wu and Chan 1997; Ding 1990; Takaya and Nakamura 2005a; 2005b; Park et al. 2016; Pang and Lu 2019; Shi et al. 2019). Among them, the advection of nega-tive vorticity, which is related to the eastward passage of a shortwave trough or the establishment of a blocking ridge upstream of the SH domain, has been documented to trig-ger downward motion over Siberia. Concurrently, the cold advection associated with the upstream circulation and the near-surface diabatic cooling can change the thicknesses of the mid-and-low–pressure fields and further lead to compen-satory downdrafts over the Siberian region. As a result, the strong subsidence and associated mass convergence in the mid–upper troposphere contributes to the rapid intensifica-tion of the SH. So far, the synoptic intensification of the SH related to cold surges has been well understood.

As a semi-permanent circulation, the SH exhibits a remarkable seasonal evolution (e.g. Chen et al. 2013). How-ever, less attention has been paid to the initial formation of the SH. Investigating the initial formation process of the SH and the associated physical mechanisms could improve our understanding of the thermodynamics underlying the SH formation and may also have implications for sub-seasonal climate predictions over East Asia. A few studies have sug-gested that the SH originates over Siberia around October and persists until the following April (Cohen et al. 2001; Panagiotopoulos et al. 2005; Tubi and Dayan 2013; Iqbal et al. 2013; Riaz and Iqbal 2017; Gao et al. 2021). How-ever, the exact formation date of the SH remains elusive.

In addition, the difference between the initial SH formation and its synoptic strengthening related to cold-surge activity needs to be clarified.

This study aims to determine the initial formation process and mechanisms of the SH. Section 2 describes the datasets and methods. Section 3 presents the climatological charac-teristics of the initial SH formation, including the circulation changes, thermal processes, and diagnostic analyses. Sec-tion 4 provides the summary and discussion.

2 Data and methods

2.1 Data

This study uses the daily and monthly atmospheric data from the Japanese 55-year Reanalysis (JRA-55) project conducted from the Japan Meteorological Agency (Kobayashi et al. 2015). This dataset is available from 1958 to 2019 and has a horizontal resolution of $1.25° \times 1.25°$ on a longitude–lati-tude grid.

2.2 Methods

Following the approach of previous studies, we select the area-averaged sea level pressure (SLP) over the key region of 70°–120°E, 40°–60°N to measure the evolution of the SH (Gong and Ho 2002; Chang and Lu 2012; Fu et al. 2022). This area generally covers the central regions of the SH and can represent the entire SH system well (Gong and Ho 2002).

Figure 1 shows the climatology of the monthly SLP evolution over the Eurasian continent from July in the year under consideration [July (0)] to June of the following year [June (1)]. The red rectangles denote the key SH regions. In July (0), the SLP over the Siberian domain is slightly lower than that in its surrounding regions. From August (0) to October (0), the SLP increases over the upstream region of Siberia and gradually spreads eastward; in October (0), the key region of SH is occupied by a high-pressure sys-tem with a maximum value above 1025 hPa over Mongo-lia–Siberia. This high-pressure system further increases and expands from October (0) to January (1), with the maximum value exceeding 1035 hPa in January (1). After that, the high-pressure system decreases continuously with its cover-age shrinking from January (1) to April (1). In May (1) and June (1), the SH nearly disappears. The annual cycle of the daily SLP averaged along the longitude belt (70°–120°E) further confirms the seasonal changes of the SH (Fig. 2). The results indicate that the SH generally forms in October and persists until the following April, with its peak in midwinter (January).
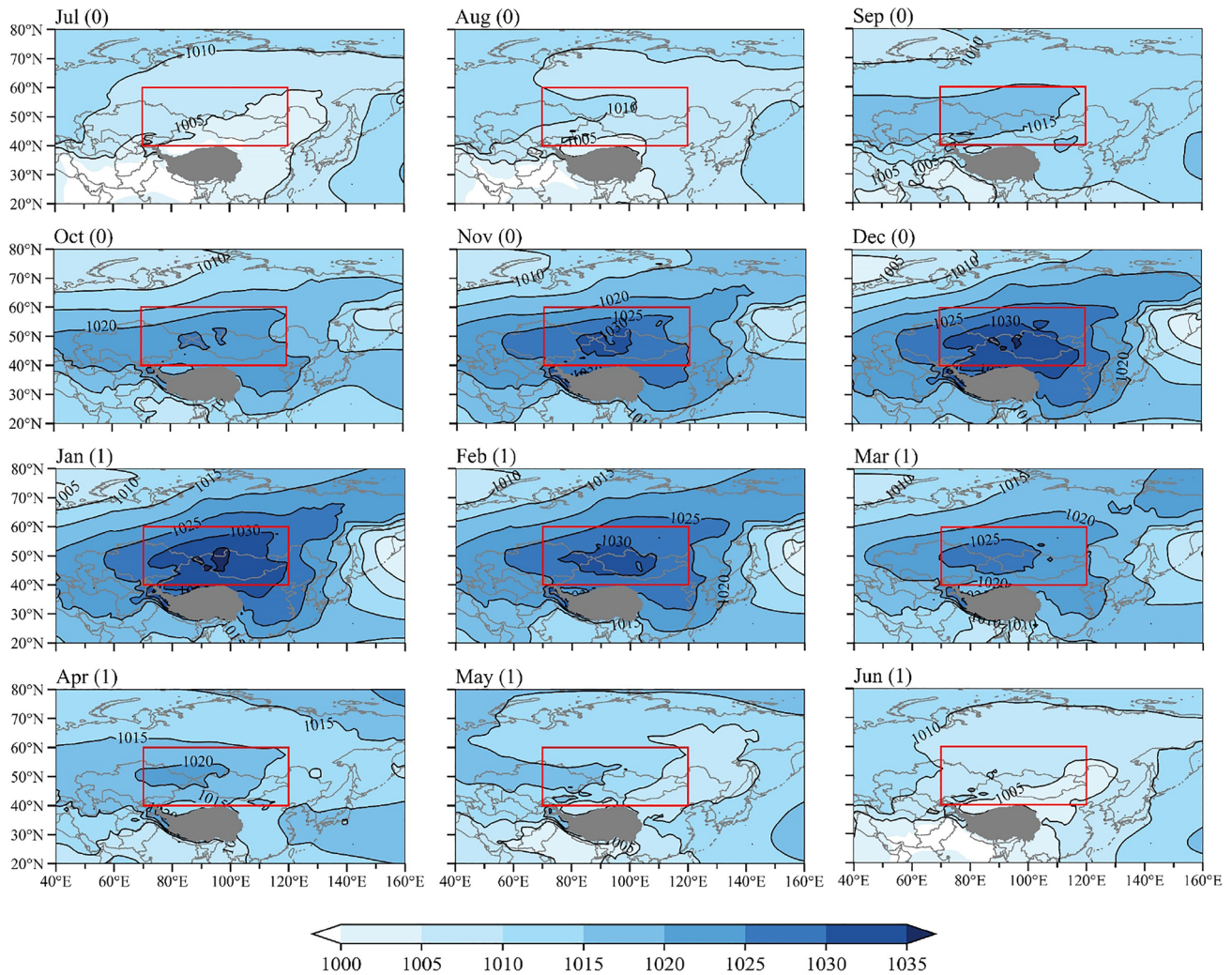
Fig. 1 The climatology of the monthly SLP evolution (shading and contours, units in hPa) from July (0) to June (1) during 1958–2019. The red rectangles indicate the key regions of the SH domain (70°–120°E, 40°–60°N)
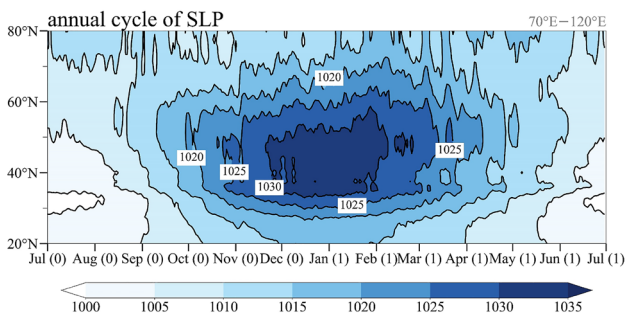

Fig. 2 The climatological latitude–time cross-section of the daily SLP evolution (shading and contours, units in hPa) along a longitude belt (70°–120°E) from July (0) to July (1) during 1958–2019

To objectively detect the date of the initial SH formation, the accumulation approach is used. This method can capture the seasonality of atmospheric variables (e.g. precipitation, OLR, and winds) and objectively detect the timing (i.e. the start and end dates) of these variables (Liebmann and Marengo 2001; Cook and Buckley 2009; Noska and Misra 2016; Bombardi et al. 2019; Chen et al. 2022; Hu et al. 2022). Here, the SLP cumulative quantity C for day n, year y is computed as:

$$C_y(n) = \sum_{i=t_0}^{n} (P_y(i) - \overline{\overline{P_C}}), \tag{1}$$

Where

$$\overline{\overline{P_C}} = \frac{1}{365 \cdot Y} \sum_{y=1}^{Y} \sum_{i=t_0}^{t_0+365} P(y,i). \qquad (2)$$

$C_y(n)$ indicates the sum of $P_y(i) - \overline{\overline{P_C}}$ from t_0 to day n in year y; $P_y(i)$ is the area-averaged (70°–120°E, 40°–60°N) daily SLP over the SH domain (SLP$_{SH}$) on day i during t_0–day n in year y; $\overline{\overline{P_C}}$ is the climatological annual average of the daily SLP$_{SH}$; the variable "Y" in Eq. (2) means the total 61 years under consideration (i.e. $Y=61$); $P_y(i) - \overline{\overline{P_C}}$ denotes the difference between the daily SLP$_{SH}$ and its climatological annual mean (SLP$_{SH}$ anomaly). The calculation should be started within the non-prevailing periods of the SH so that the formation days are never missed. In this study, the initial day (i.e. t_0) for calculation is July 1, which is during the periods with the lowest SLP$_{SH}$ during a climatological year. If SH formation is considered to occur on the day on which the SLP$_{SH}$ stably exceeds its climatological annual mean (i.e. 1018.7 hPa), the minimum point of the cumulative quantity C indicates the SH formation date. Figure 3a shows an example for the application of Eq. (1). Since we start the calculation of C on July 1, the SLP$_{SH}$ anomaly (black line in Fig. 3a) is initially negative, and the quantity C (blue line in Fig. 3a) exhibits a downward trend. Once the SLP$_{SH}$ stably exceeds its climatological annual

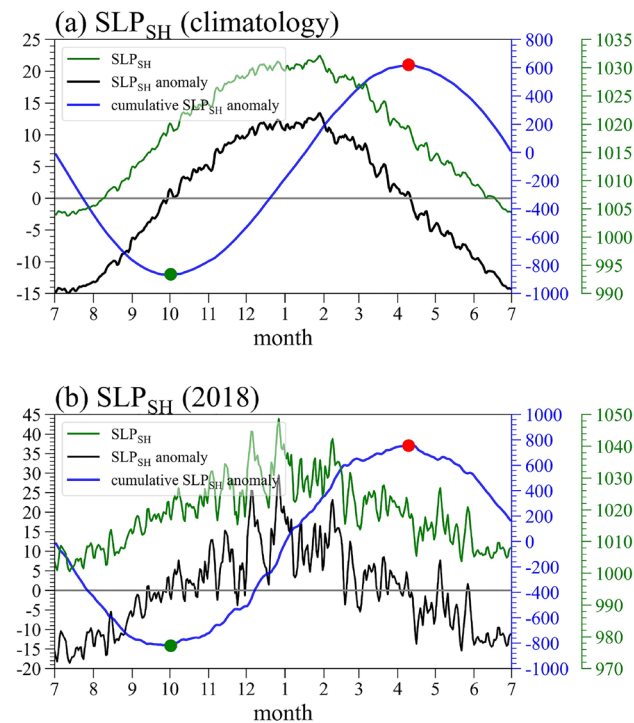**(a) SLP$_{SH}$ (climatology)**

(b) SLP$_{SH}$ (2018)

Fig. 3 The daily time series of the area-averaged SLP (SLP$_{SH}$, green lines; units in hPa), SLP$_{SH}$ anomaly (black lines; units in hPa), and cumulative SLP$_{SH}$ anomaly (blue lines; units in hPa) in **a** the climatology and **b** 2018 within the study region (70°–120°E, 40°–60°N). The green and red dots denote the minimum and maximum of the cumulative SLP anomaly, respectively

mean, the SLP$_{SH}$ anomaly would be observed as a positive value, and the cumulative value C would alter its signal from descending to ascending, reaching its minimum for the climatological year. As such, the absolute minimum point of C is considered to be the SH formation date. Similarly, the absolute maximum point of C indicates the demise of the SH (i.e., the day on which the SLP$_{SH}$ is stably less than its climatological annual mean). Thus, the initial formation date of SH can be objectively detected in the climatology and in any individual years. It should be noted that this method can successfully overcome the fluctuations in SLP$_{SH}$ during an individual year. For example, even though the SLP$_{SH}$ (green line) and the SLP$_{SH}$ anomaly (black line) exhibit notable fluctuations in 2018, the curve C evolves steadily and shows distinct alternations from descending to ascending, as shown in Fig. 3b. To the best of authors' knowledge, this is probably the first time to propose and define the date of the SH formation.

The SH formation dates are computed from 1958 to 2018 based on the accumulation approach (Table 1). Then, the climatological mean SH formation date is obtained on the basis of calculating the average of SH formation date in each year. In the climatology, the SH forms on October 1 (55th pentad). In order to filter synoptic noises, we transform the dates into pentad series. The 73-pentad mean data are constructed from the daily data for each year, with the leap day omitted. In addition, climatological composited mean data are utilized to highlight the climatic characteristic of SH formation. We determine P_0 (i.e. the SH formation pentad) for every individual year and obtain the features based on the average of changes around P_0 in individual years. In the following, the P_{-1}, P_0, and P_{+1} denote one pentad before, during, and after the SH formation, respectively.

When analyzing the thermal processes, the atmospheric diabatic heating regime is designated by the apparent heat source determined via the inverse calculation scheme deduced by Yanai et al. (1973). As shown in Eq. 3, the diabatic heating rate (Q_1, units in K s^{-1}) is performed as:

$$Q_1 = \frac{\partial T}{\partial t} + \vec{V} \cdot \nabla T + \left(\frac{p}{p_0} \right)^{\frac{R}{c_p}} \omega \frac{\partial \theta}{\partial p}. \qquad (3)$$

Following Bluestein (1993) and Holton and Hakim (2013), we adopt the quasi-geostrophic omega equation to diagnose the formation mechanisms of the SH:

$$\left(\sigma \nabla^2 + f_0^2 \frac{\partial^2}{\partial p^2} \right) \omega = f_0 \frac{\partial}{\partial p} \left[\vec{V_g} \cdot \nabla (f + \xi_g) \right]$$
$$- \nabla^2 \left[\vec{V_g} \cdot \nabla \frac{\partial \phi}{\partial p} \right] - \frac{R}{c_p p} \nabla^2 \frac{dQ}{dt}. \qquad (4)$$

We then write the equation as:

$$S = S_1 + S_2 + S_3,$$

Table 1 The time of SH formation from 1958 to 2018

The time of the Siberian High formation from 1958 to 2018											
Year	Date	Pentad	Year	Date	Pentad	Year	Date	Pentad	Year	Date	Pentad
1958	Sep 22	53	1974	Sep 30	55	1990	Oct 6	56	2006	Oct 15	58
1959	Oct 12	57	1975	Oct 10	57	1991	Sep 30	55	2007	Sep 22	53
1960	Sep 26	54	1976	Oct 20	59	1992	Oct 1	55	2008	Sep 22	53
1961	Oct 9	57	1977	Oct 2	55	1993	Sep 29	55	2009	Oct 3	56
1962	Sep 22	53	1978	Sep 30	55	1994	Sep 29	55	2010	Oct 12	57
1963	Sep 21	53	1979	Sep 18	53	1995	Oct 18	59	2011	Sep 26	54
1964	Sep 30	55	1980	Oct 2	55	1996	Oct 2	55	2012	Sep 26	54
1965	Oct 3	56	1981	Oct 5	56	1997	Sep 8	51	2013	Oct 11	57
1966	Oct 3	56	1982	Oct 9	57	1998	Oct 11	57	2014	Sep 27	54
1967	Sep 27	54	1983	Oct 8	57	1999	Sep 27	54	2015	Oct 6	56
1968	Sep 16	52	1984	Oct 14	58	2000	Sep 27	54	2016	Oct 2	55
1969	Sep 20	53	1985	Oct 10	57	2001	Oct 10	57	2017	Sep 25	54
1970	Sep 22	53	1986	Oct 1	55	2002	Oct 16	58	2018	Sep 26	54
1971	Sep 13	52	1987	Oct 6	56	2003	Sep 24	54			
1972	Sep 17	52	1988	Sep 24	54	2004	Sep 23	54			
1973	Sep 28	55	1989	Sep 30	55	2005	Sep 30	55			

$$S = \left(\sigma \nabla^2 + f^2 \frac{\partial^2}{\partial p^2} \right) \omega \propto -A^2 \omega,$$

$$S_1 = f \frac{\partial}{\partial p} \left[\overrightarrow{V_g} \cdot \nabla (f + \xi_g) \right],$$

$$S_2 = -\nabla^2 \left[\overrightarrow{V}_g \cdot \nabla \frac{\partial \phi}{\partial p} \right] = \nabla^2 \left[\frac{R}{p} \overrightarrow{V}_g \cdot \nabla T \right],$$

$$S_3 = -\frac{R}{c_p p} \nabla^2 \frac{dQ}{dt}.$$

The term on the left-hand side of Eq. 4 is the Laplacian of omega (called Term S) and is approximately equivalent to omega multiplied by a negative coefficient ($-A^2 \omega$). Here, "A^2" indicates any value that is positive, as such the value "$-A^2$" would be a negative coefficient, making the Term S more concise. The terms on the right-hand side are the vertical differential of the geostrophic absolute vorticity advection (called Term S_1), the Laplacian of the geostrophic temperature advection (called Term S_2), and the Laplacian of the atmospheric diabatic heating (called Term S_3).

The two-sided Student's t-test is applied to assess the statistical significance of the composited differences.

3 Results

3.1 Evolution of the atmospheric circulation associated with the SH formation

Figure 4 presents the evolution of the composited SLP and 850-hPa winds during the SH formation periods. Before the SH formation (Fig. 4a–b), obvious westerly winds are observed over north Eurasia with an eastward extension to the Far East. There is a signal of a high-pressure center in the upstream region, expanding and spreading eastward to the SH domain. In the pentad of SH formation (i.e. P_0), an evident high arises in the SH region, with its central pressure exceeding 1024 hPa. The center of the SH further intensifies and expands to the surrounding continent (Fig. 4c–d). One pentad after the SH formation (Fig. 4d), the Eurasian continent is entirely dominated by the high, which is generally larger than 1018 hPa over the land, with its largest center residing over the SH domain. In addition, there is a branch of northerly winds intruding southward to the subtropics over coastal Asia. It is interesting to note that, after its formation (i.e., P_0), the high does not spread eastward anymore, but rather, further amplifies over the local region of the SH (Fig. 4c–d). Figure 4e shows the longitude–time cross-section of the SLP along the latitude belt (40°–60°N) from 10 pentads before to 10 pentads after the SH formation.
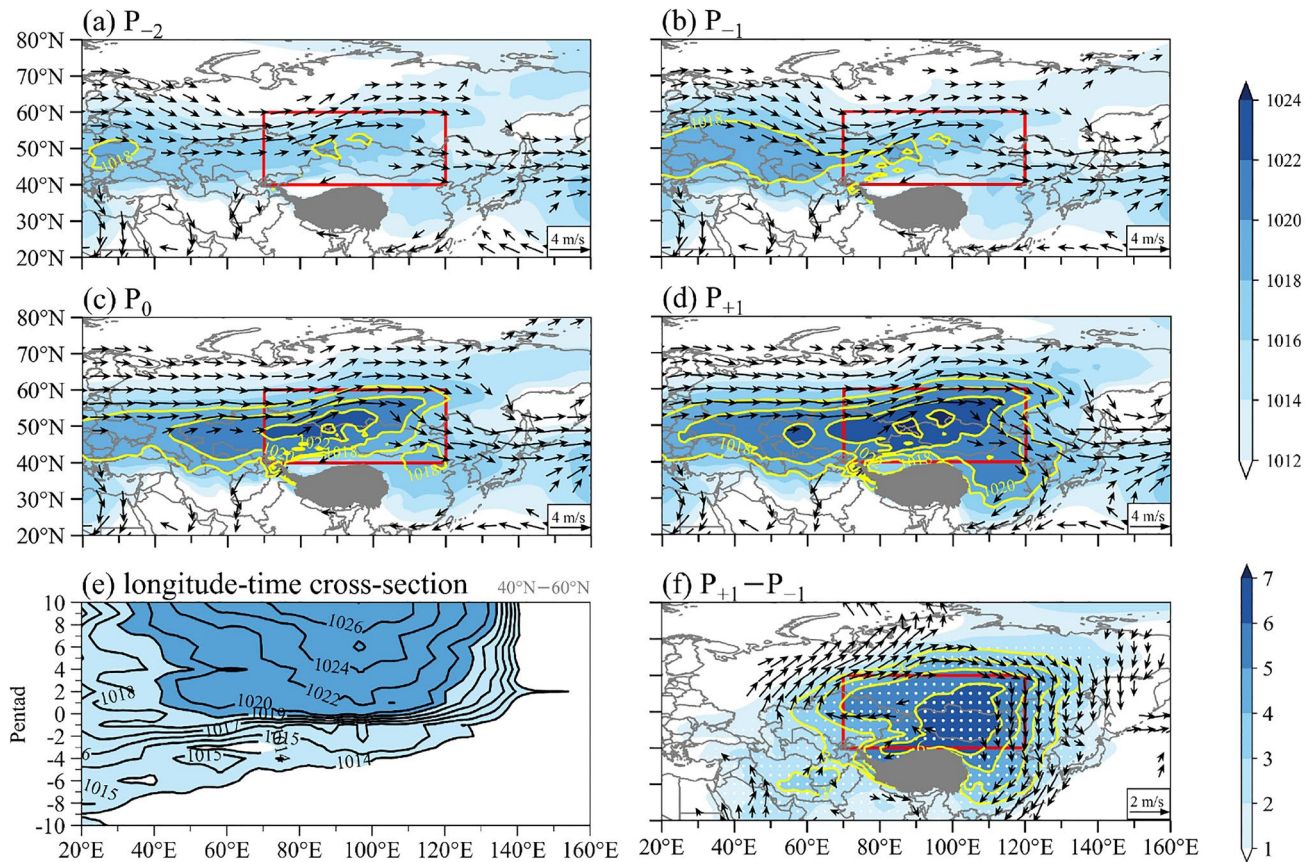
Fig. 4 **a–d** The climatology of the composited SLP (shading and contours; units in hPa) and 850-hPa winds (vectors; units in m s^{-1}) from two pentads prior to Siberian High (SH) formation to one pentad afterwards. Only the winds larger than 3 m s^{-1} are shown in (**a**)–(**d**). **e** The longitude–time cross-section of the composited SLP (contours and shadings; units in hPa) along the latitude belt (40°–60°N) from 10 pentads before the SH formation to 10 pentads after. The light-blue and dark-blue shadings indicate SLP values lower and higher than 1019 hPa, respectively. **f** The difference between (**d**) and (**b**), including the SLP (those significant at the 95% confidence level are dotted) and 850-hPa winds (only those larger than 1 m s^{-1} and those significant at the 95% confidence level are shown), which can reveal the largest changes during the SH formation periods. The red rectangles denote the key region of the SH domain (70°–120°E, 40°–60°N)

It can be seen clearly that the high-pressure center upstream is moving eastward from P_{-10} to P_0, increasing the SLP_{SH} and favoring the establishment of SH. After its formation (P_0 to P_{10}), the high stops propagating, with its center located around 100°E. This occurrence may thereby verify the definition of SH formation; that is, after P_0, the primary eastward-spreading center stops in the SH region, and the high subsequently grows.

In addition, considering that the SLP_{SH} presents a sharp increase from P_{-1} to P_{+1} (Fig. 4b–e), we examine the differences in the SLP and 850-hPa winds between P_{+1} and P_{-1} as well (Fig. 4f). The difference map shows that the SLP is significantly increased in most areas of Eurasia, with a center located in the central region of the SH. Concurrently, an anomalous anticyclonic circulation appears to the east of the Ural Mountains, accompanying strong anomalous northerlies over East Asia. It can be concluded that the SH exhibits rapid and also significant

strengthening from P_{-1} to P_{+1}. Therefore, we focus on analyzing this period.

Figures 5a–c display the climatology of the 500-hPa geopotential height as well as its deviation relative to the zonal mean during P_{-1}, P_0, and P_{+1}, respectively. The difference between P_{+1} and P_{-1} is shown in Fig. 5d. During the SH formation periods (Fig. 5a–c), the ridge centered over the Scandinavian Peninsula expands from western Eurasia to the SH area, and the low trough residing over the coast of Northeast Asia deepens. The difference map shows a marked northeast–southwest-oriented ridge over the East European Plain extending eastward to central Siberia (Fig. 5d). Meanwhile, there is a deep trough over East Asia with a northeastward extension to the Sea of Okhotsk. The evolution of the 200-hPa geopotential height (not shown) is similar to that at 500 hPa, indicating a barotropic structure of the SH-related atmospheric anomalies in the troposphere. We have also examined the westerly jet over the subtropical western
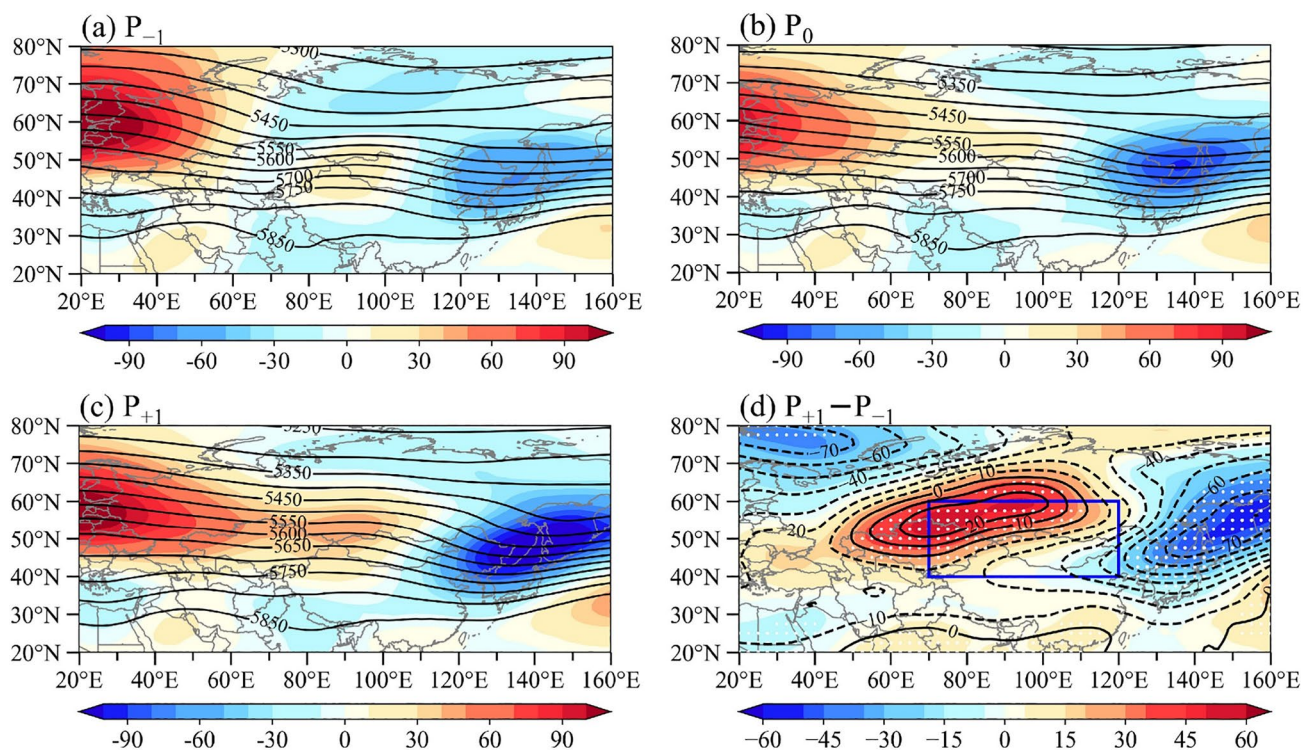
Fig. 5 The climatology of the original 500-hPa geopotential height (contours; units in gpm) and its deviation from the zonal mean for one pentad **a** before, **b** during, and **c** after the SH formation. **d** The difference between (**c**) and (**a**), including the original 500-hPa geo-potential height and its deviation (those significant at the 95% confidence level are dotted). The blue rectangle in (**d**) denotes the key region of the SH domain (70°–120°E, 40°–60°N)

North Pacific. Results show that the westerly jet accelerates and intrudes southward during the SH formation periods (not shown).

We further examine the vertical structure of the atmospheric circulation related to the SH formation. Previous studies (Chen et al. 2014; Huang et al. 2018; Hu et al. 2019) have indicated that it is more appropriate to use divergent winds (directly associated with vertical motion) to depict the vertical circulation. Since the vertical circulation exhibits meridional differences, we provide zonally averaged values (70°–120°E) here. Figure 6 displays the climatology of the composited zonal winds, divergent meridional winds, and vertical velocities during the SH formation periods. Noting that the downward (southward) vectors denote the downward motion (southerly divergent winds) and vice versa. Before SH formation (Fig. 6a), the entrance of the subtropical westerly jet is located over the south of the Mongolian Plateau, accompanied by a secondary circulation extending from the subtropics to the midlatitudes. This secondary circulation features descending motion as well as mass convergence to the south of the SH areas. The westerly jet migrates southward with its amplitude increasing in P_0; correspondingly, the secondary circulation also amplifies. After one pentad of SH formation (Fig. 6c), distinct descending motions

dominate almost the entire SH area, along with a strong convergence (divergence) center over the upper (lower) troposphere. Meanwhile, a meridional circulation in the opposite direction occurs to the north of the secondary circulation. From Fig. 6d (difference map), the westerly winds are accelerated over the subtropical regions while they are decelerated over the SH area, indicating southward movement and strengthening of the subtropical westerly jet. To its north, zonal winds over higher latitudes are enhanced, and an anomalous meridional circulation appears with its center located around 60°N in the middle troposphere, which may be a response to the southward shift and enhancement of subtropical westerly jet. Overall, the secondary circulation of the subtropical westerly jet is conducive to the dominant downdraft over the SH, thus contributing to SH formation.

3.2 Changes in the thermal process during the SH formation period

Considering that the SH is only characterized as a high but also features cold airmass pooling (Hasanean et al. 2013; Liu and Zhu 2020), the thermal processes for SH formation are also examined in Fig. 7. Figures 7a–c display the evolution of the temperature advection, diabatic heating, and
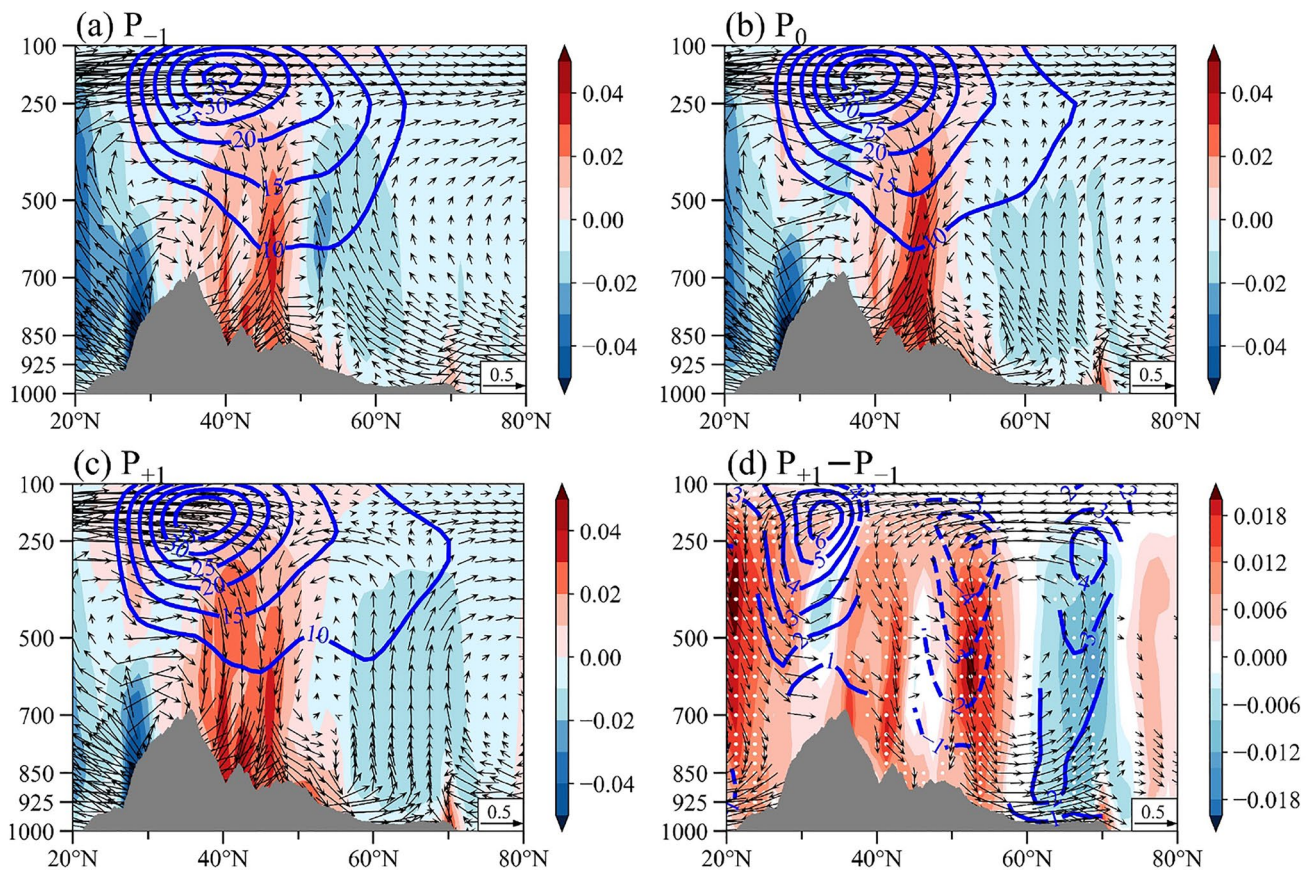
Fig. 6 The climatology of the local meridional circulation cell, depicted by the vertical velocities (shading and vectors; units in Pa s^{-1}), the divergent meridional winds (vectors; units in m s^{-1}), and the zonal winds (contours; units in m s^{-1}) averaged over 70°–120°E for one pentad **a** before, **b** during, and **c** after the SH formation. **d** The difference between (**c**) and (**a**). Only the zonal winds larger than 10 m s^{-1} are shown in (**a**–**c**). Only the significant differences (at the 95% confidence level) of the vertical velocities, divergent meridional winds, and zonal winds are shown in (**d**). The vertical velocities that are significant at the 95% confidence level are also dotted in (**d**)

air temperature in P_{-1}, P_0, and P_{+1}, respectively. The difference between P_{+1} and P_{-1} is shown in Fig. 7d. During the SH formation periods (Fig. 7a–c), cold advection over the SH domain is enhanced in all layers with a center of action locating over the upper troposphere. The diabatic heating over the southern SH is negative and exhibits slight changes during P_{-1}–P_{+1}. The opposite is true over the northern SH region: the diabatic heating in the middle troposphere is positive in P_{-1}, weakening and changing into negative values along with SH formation (Fig. 7a–c). Such a thermal structure is conducive to a decrease in air temperature. In the difference fields, centers of anomalous cold advection and diabatic cooling appear over the upper and middle troposphere, respectively. An anomalous cold center is observed over the lower levels of the SH region, indicating the gathering of cold airmasses (Fig. 7d).

It is interesting to note that, during the SH formation periods, the diabatic cooling appears to be weak and exhibits little change near the surface of the SH. It seems that the impacts of lower-level diabatic cooling for SH formation is

not as important as it is for the synoptic intensification of SH that is associated with a cold surge (Ding and Krishnamurti 1987; Takaya and Nakamura 2005a; Pang and Lu 2019). To further verify the role of diabatic heating, we examine the main components of the diabatic heating rate (i.e. the sensible heating rate, shortwave radiative heating rate, longwave radiative heating rate, and condensation heating rate) separately, and the results are provided as follows. During the SH formation periods, even though the longwave radiation from the surface is negative, the sensible heating is prominent and largely counteracts the effects of the radiative cooling (not shown). Figure 8a–c provide the 850-hPa sensible heating rate (depicted by the vertical diffusion heating rate; positive values indicate the surface is heating the atmosphere) and the temperature differences between the surface and 850 hPa ($T_s - T_{850}$) in P_{-1}, P_0, and P_{+1}, respectively. Figure 8d shows the difference between P_{+1} and P_{-1}. During the SH formation periods (Fig. 8a–c), the sensible heating is distinct over the Mongolian Plateau as well as the Iranian Plateau, and the surface temperature is significantly higher than the
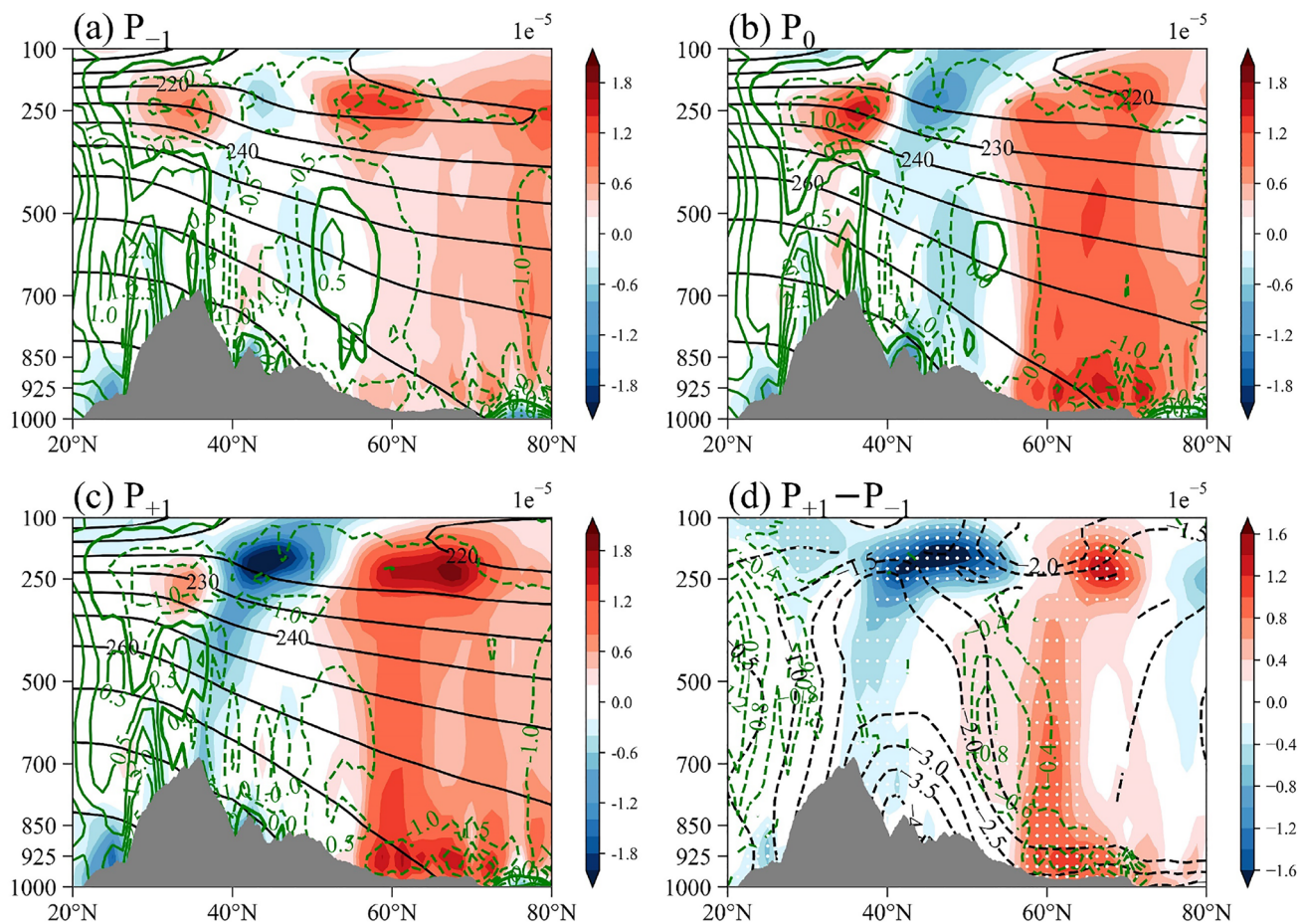
Fig. 7 The climatology of the local meridional thermal process, depicted by the temperature (black contours; units in K), the diabatic heating rate (green contours; units in K s⁻¹), and the temperature advection (shading, units in K s⁻¹) averaged over 70°–120°E for one pentad **a** before, **b** during, and **c** after the SH formation. **d** The difference between (**c**) and (**a**). Only significant differences (at the 95% confidence level) of the temperature and diabatic heating rate are shown in (**d**). The differences in temperature advection that are significant at the 95% confidence level are dotted in (**d**)

atmospheric temperature over the SH domain is. Due to the terrain of the Tibetan Plateau and Mongolian Plateau, cold airmasses from higher latitudes cannot migrate farther southward and instead sink over the SH area. The gathering of colder air actively promotes vertical heat exchanges between the surface and the lower-level air, subsequently cooling the local surface. The sensible heating from the surface is therefore evident and counteracts the radiative cooling. For the differences between P_{+1} and P_{-1} (Fig. 8d), both the sensible heating and $T_s - T_{850}$ are decreased. It can be inferred from Fig. 8d that the local surface of the SH is cooled and the differences between T_s and T_{850} ($T_s - T_{850}$) are reduced due to the existence of terrain and the gathering of cold advective airmasses, thus suppressing the vertical diffusive heating rate. The local surface is assumed to be in a passive position during the thermal process of SH formation.

Based on the qualitative analysis above, we assume that diabatic cooling may play a minor role in driving the SH

formation. In order to verify our hypothesis, we further apply the omega equation to quantitatively diagnose the contributions of the thermal and dynamic processes to SH formation in the next section.

3.3 Diagnosing the SH formation

Figure 9 shows the climatology of the composited SLP, divergence, and vertical velocity from 10 pentads before to 10 pentads after SH formation. Noting that the SH is mainly located over the Mongolian Plateau, data below the height of the terrain is masked. Figure 9a shows that the SLP exhibits the sharpest increase from P_{-1} to P_{+1}, which is consistent with the main results demonstrated in Fig. 4. The increase in SLP can be attributed to two separate terms: the vertically integrated divergence and the vertically integrated density advection (He 2012). Also, considering that the former is an order of magnitude
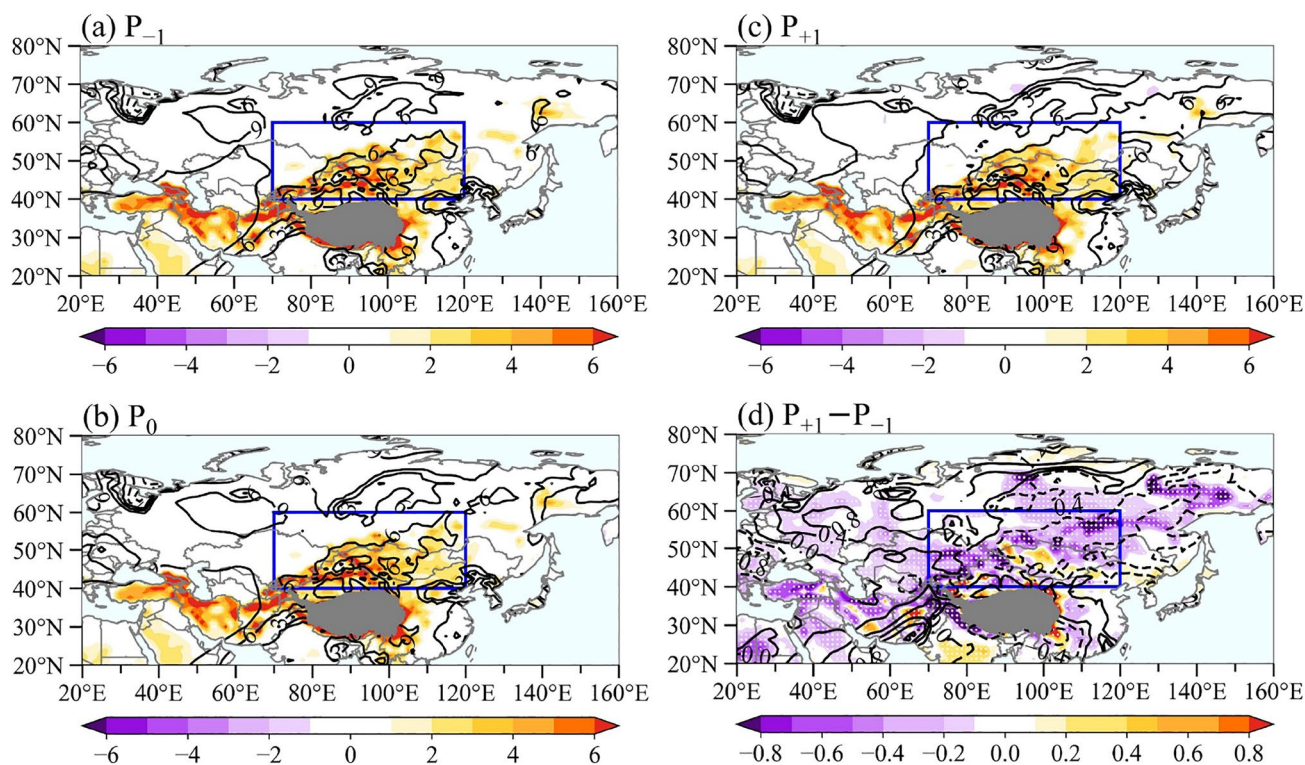
Fig. 8 The climatology of the 850-hPa vertical diffusion heating rate (shading; units in K s^{-1}) and the difference between the 850-hPa temperature and surface temperature ($T_s - T_{850}$, contours; units in K) for one pentad **a** before, **b** during, and **c** after the SH formation. **d** The difference between (**c**) and (**a**), including the 850-hPa vertical diffu- sion heating rate (those significant at the 95% confidence level are dotted) and $T_s - T_{850}$ (only those significant at the 95% confidence level are shown). The blue rectangles denote the key region of the SH domain (70°–120°E, 40°–60°N)

larger than the latter, we focus on analyzing the divergence term hereafter. It can be seen clearly from Fig. 9b that the air convergence in the upper troposphere significantly increases from P$_{-1}$ to P$_{+1}$, directly leading to the net air convergence above the SH and thus contributing to the SH formation.

According to the continuity equation, the convergence in the upper troposphere is always accompanied by downward motion. Therefore, the associated vertical velocity is also presented in Fig. 9c. The sinking motion appears to become enhanced while the center of action is in the middle–upper troposphere from P$_{-1}$ to P$_{+1}$ and remains stable after P$_{+1}$. Due to the inherent coupling between the downward motion and the air convergence, we further investigate the quasi-geostrophic omega equation (Holton and Hakim 2013). Figure 10 represents the vertical velocity and each term of the omega equation (Eq. 4) multiplied by −1 (i.e., −S$_1$, −S$_2$, and −S$_3$) in P$_{-1}$, P$_0$, P$_{+1}$, respectively, as well as their differences between P$_{+1}$ and P$_{-1}$. Here, the terms −S$_1$, −S$_2$, and −S$_3$ denote the contributions of the vertical differential of geostrophic absolute vorticity advection, the Laplacian of geostrophic temperature advection, and the Laplacian of atmospheric diabatic

heating, respectively. The descending motion is significantly strengthened in all layers, with a center of downward action in the middle–upper levels from P$_{-1}$ to P$_{+1}$ (Fig. 10a). All terms on the right-hand side have changed with different degrees form P$_{-1}$ to P$_{+1}$ (Fig. 10b–d). Among them, a notable shift mainly occurs in term −S$_1$. The difference fields reveal that the Term −S$_1$ mainly contributes to the prominent downdraft in the middle troposphere (Fig. 10e). Although −S$_2$ and −S$_3$ are significant in the upper troposphere, they are largely counteracted by −S$_1$. Besides, −S$_1$ and −S$_2$ in the lower levels are also conducive to the descending motion, and −S$_3$ can favor mid-level downdrafts and lower-level updrafts, respectively (Fig. 10e). These terms support our hypothesis that diabatic heating plays a minor role in driving SH formation (Fig. 6).

It can also be concluded that the SH is driven mainly by dynamic processes. The vertical differential of the geostrophic absolute vorticity advection in the mid–upper levels largely contributes to the strong descending motion during SH formation. The accompanying convergence in the upper troposphere favors the net accumulation of airmasses above the SH region, resulting in SH formation.
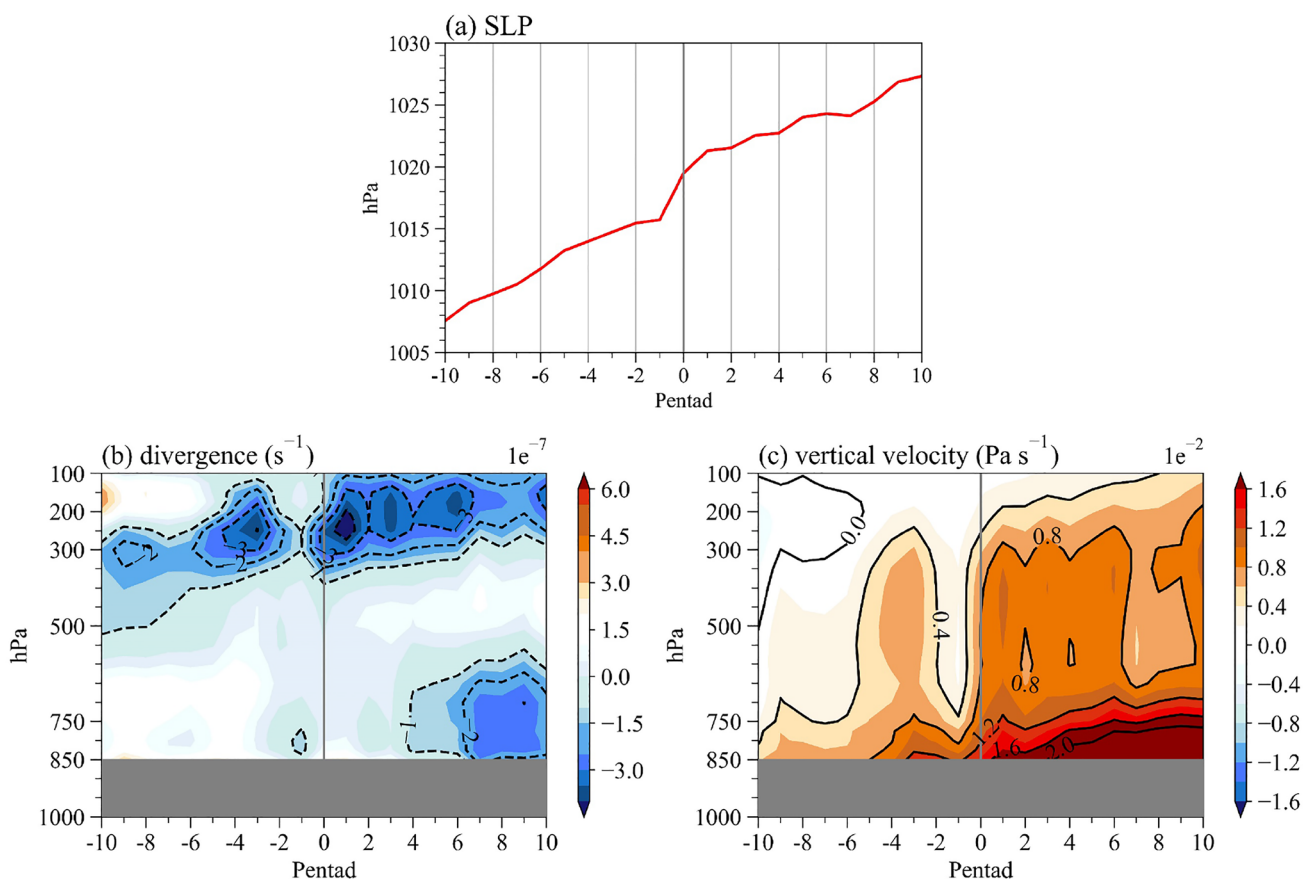
Fig. 9 The climatology of the composited **a** SLP (units in hPa), **b** divergence (units in m s^{-1}), and **c** vertical velocity (Pa s^{-1}) from 10 pentads before SH formation to 10 pentads after. All are averaged in the key SH study region (70°–120°E, 40°–60°N). The topography over the key region is masked with gray shadings

4 Summary and discussion

Based on the area-averaged SLP over the SH domain (70°–120°E, 40°–60°N), we applied the absolute minimum of the cumulative SLP anomaly to objectively detect the SH formation dates from 1958 to 2018. We then used composited climatological data to reveal the changes in the three-dimensional circulation and thermal processes during the SH formation periods. Furthermore, we utilized the quasi-geostrophic omega equation to quantitively diagnose the main contributor to SH formation.

Figure 11 summarizes the difference fields before and after SH formation. In the lower levels, an anticyclonic circulation dominates the Eurasian continent. Due to the slope of the Tibetan Plateau, the cold airmasses from higher latitudes gather over the SH domain, cooling the local surface and promoting heat exchange over the SH area. The sensible heating from the surface is therefore strong and largely offsets the radiative cooling, resulting in weak diabatic cooling during the SH formation periods. In the middle troposphere, a northeast–southwest-oriented ridge and trough appear over the Ural Mountains and the coast of Northeast Asia, respectively. The cold advection and negative vorticity advection in the front of the ridge (in the rear of the trough) are conducive to the sinking motion and airmass convergence over the SH. In the 200-hPa field, there exists a ridge and a trough with the same positions and orientations as those in the 500-hPa field. The subtropical westerly jet also intensifies continuously and migrates southward from the Mongolian Plateau to the north of the Tibetan Plateau. Concurrently, the jet-associated secondary circulation strengthens and expands over the area south of the SH region. To its north, an inverted meridional circulation appears, which can be seen as a response to the southward shift and enhancement of subtropical westerly jet. The downward branches of these two circulations favor large-scale subsidence and upper-level convergence over the Siberian region.

Due to the inherent coupling between the air convergence and sinking motion, we utilized the omega equation to quantitively diagnose the effects of thermodynamic factors to the SH formation. Further diagnosis reveals that the vertical differential of the geostrophic absolute vorticity
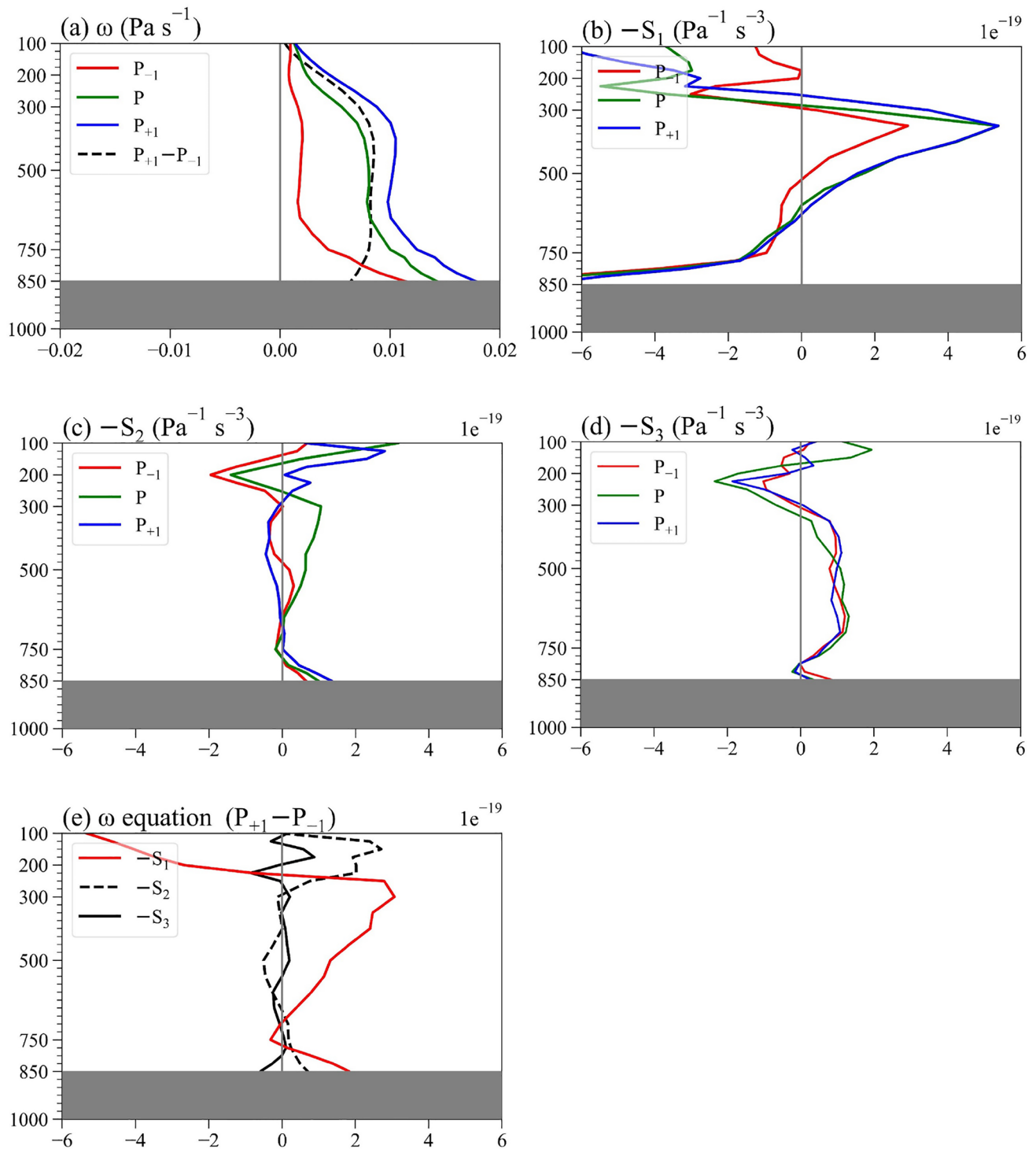
Fig. 10 The diagnosis of the quasi-geostrophic ω equation, including **a** the vertical velocity (ω, units in Pa s⁻¹), **b** the vertical differential of the geostrophic absolute vorticity advection (Term −S₁), **c** the Laplacian of the geostrophic temperature advection (Term −S₂), **d** the Laplacian of the atmospheric diabatic heating (Term −S₃) multiplied by −1 in one pentad before, during, and after the SH formation, and **e** the difference in −S₁, −S₂, and −S₃ between one pentad before and after SH formation. The topography over the key region is masked with gray shadings
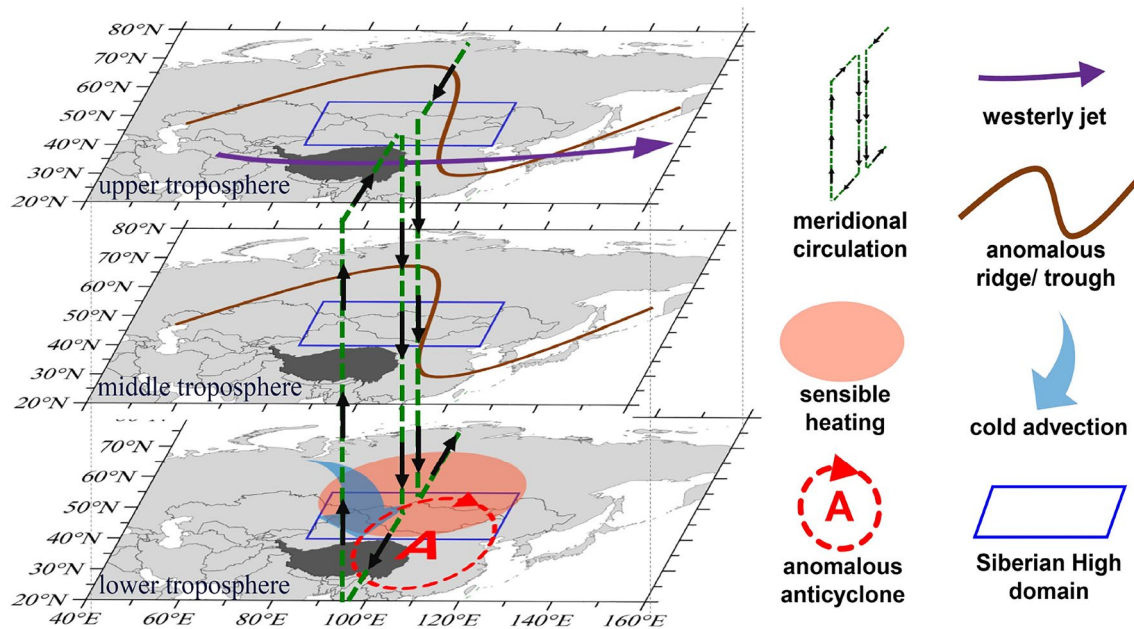
Fig. 11 Schematic diagram of the three-dimensional atmospheric circulation and thermal processes in association with the SH formation

advection is the main contributor to the sinking motion, and the Laplacian of the geostrophic temperature advection as well as the Laplacian of the atmospheric diabatic heating are less important. The strong upper-level convergence associated with the downdraft accounts for the net accumulation of airmasses above the SH domain, therefore leading to SH formation. We therefore reach the conclusion that SH formation is driven mainly by dynamic processes.

The dates of SH formation are objectively detected, and its climatological features are clearly represented herein. Our analysis is likely the first to propose and investigate the formation of the SH, which will lead to a deeper understanding of the SH seasonality as well as the mechanisms behind it. We also noted that the SH synoptic amplification associated with cold surges and the initial SH formation are different processes that should be clearly distinguished in the future. In midwinter, due to the presence extensive snow cover over the Eurasian continent, the surface is too cold to be passively cooled by the air; the opposite is true during SH formation periods, when narrow range of snow cover leads the surface to be passively cooled by the air (Cohen et al. 2001; Zhang et al. 2017; Luo and Wang 2019). The difference between T_s and T_{850} is less (more) significant, and the sensible heating from the surface is much weaker (stronger) in the winter (SH formation periods) (Fig. 8). Additionally, the extensive (narrow) range of snow cover in the winter (SH formation periods) can reduce (enhance) downward shortwave radiation and enhance (reduce) the upward radiative cooling (Cheng et al. 2022; Wu and Ding 2022). The combined effects of

stronger (weaker) radiative cooling and weaker (stronger) sensible heating largely result in strong (weak) net diabatic cooling during midwinter (SH formation periods).

Certainly, there are still some interesting points that deserve further discussion:

(1) Why the previous eastward-spreading center of high pressure stops in the SH region and develop here after P_0 (Fig. 4e)?

It could probably be attributed to the development of mid- and upper level circulation, the terrain of Tibetan Plateau, and the development of snow cover. During $P_{-10}-P_{-1}$, short-wave troughs/ridges continuously propagate eastward, the associated absolute vorticity advection and cold advection would favor the downward motion and the air convergence, thus resulting in the eastward-spreading center of high pressure. These short-wave troughs/ridges would also consistently merge into and strengthen the ridge (low trough) over the upstream (downstream) of the SH area. In P_0, the ridge (low trough) over the upstream (downstream) amplifies to dominate the SH area, and such circulation pattern is too wavy to facilitate the spreading and passing of short-wave troughs/ridges. Therefore, eastward-spreading center of high pressure stops in the SH region. After P_0, the cold advection and negative vorticity advection in the front (rear) of the ridge (trough) favor the sinking motion and airmass convergence over the SH, making the center of high pressure develops in the SH region. Also, the secondary circulation associated with the southward movement and strengthening of subtropical westerly jet would be conducive to the

downdraft and net air mass convergence over the SH region, favoring the development of high pressure.

In addition, it is noteworthy that the terrain of Tibetan Plateau and snow cover play a role in developing the SH after its formation as well. The terrain of Tibetan Plateau would hinder the southward migration of cold advection, and such process would decrease the temperature differences between air and surface as well as the sensible heating. Also, the extensive range of snow cover would help to increase the radiative cooling near the surface of SH region. Therefore, the decrease in sensible heating with regard to the terrain of Tibetan Plateau and the increase in radiative cooling due to the presence of snow cover would be helpful to further development of SH after its formation.

(2) Do dynamic factors still play a dominant role in maintaining and developing the SH after its formation?

The present study reaches a conclusion that the SH formation is driven mainly by dynamic processes. However, the extent to which dynamic and thermal factors contribute to SH maintenance after its formation remain unclear. It is also unclear whether thermal processes still play a minor role in SH maintenance after its formation. After the period of SH formation, the surface is largely cooled by the cold advective airmass, and such a process leads to weaker sensible heating. Meanwhile, the radiative cooling is significantly intensified due to the growth of snow cover. The weakened sensible heating and enhanced radiative cooling can favor strong diabatic cooling near the surface, contributing to some degree of SH maintenance.

Declarations

Conflict of interest The authors declare that they have no conflict of interest.

Consent for publication Written information consent for publication was obtained from all participants.

Ethics approval and consent to participate Not applicable.

References

Bluestein HB (1993) Synoptic-dynamic meteorology in midlatitudes. Oxford University Press, New York

Bombardi RJ, Kinter JL, Frauenfeld OW (2019) A global gridded dataset of the characteristics of the rainy and dry seasons. Bull Am Meteorol Soc 100:1315–1328

Chang C-P, Lu M-M (2012) Intraseasonal predictability of Siberian High and East Asian winter monsoon and its interdecadal variability. J Clim 25:1773–1778

Chen W, Graf HF, Huang RH (2000) The interannual variability of East Asian winter monsoon and its relation to the summer monsoon. Adv Atmos Sci 17:48–60

Chen W, Feng J, Wu RG (2013) Roles of ENSO and PDO in the link of the East Asian winter monsoon to the following summer monsoon. J Clim 26:622–635

Chen S, Wei K, Chen W, Song L (2014) Regional changes in the annual mean Hadley circulation in recent decades. J Geophys Res Atmos 119:7815–7832

Chen L, Chen W, Hu P et al (2022) Climatological characteristics of the East Asian summer monsoon retreat based on observational analysis. Clim Dyn 60:3023–3037. https://doi.org/10.1007/s00382-022-06489-6

Cheng F, Li Q, Wang J et al (2022) Interdecadal variability of spring Eurasian snowmelt and its impact on eastern China summer precipitation. Front Earth Sci 10:927876

Cheung HHN, Zhou W (2016) Simple metrics for representing East Asian winter monsoon variability: urals blocking and western Pacific teleconnection patterns. Adv Atmos Sci 33:695–705

Cheung HN, Zhou W, Mok HY, Wu MC (2012) Relationship between Ural-Siberian Blocking and the East Asian Winter Monsoon in Relation to the Arctic Oscillation and the El Nino–Southern Oscillation. J Clim 25:4242–4257

Cohen J, Saito K, Entekhabi D (2001) The role of the Siberian High in northern hemisphere climate variability. Geophys Res Lett 28:299–302

Cook BI, Buckley BM (2009) Objective determination of monsoon season onset, withdrawal, and length. J Geophys Res Atmos 114(D23):D23109

Dai G, Mu M (2020) Arctic influence on the Eastern Asian cold surge forecast: a case study of January 2016. J Geophys Res Atmos. https://doi.org/10.1029/2020JD033298

Ding Y (1990) Build-up, air mass transformation and propagation of Siberian high and its relations to cold surge in East Asia. Meteorl Atmos Phys 44:281–292

Ding Y, Krishnamurti TN (1987) Heat budget of the Siberian High and the winter monsoon. Mon Weather Rev 115:2428–2449

Dong Z, Wang L, Yang R et al (2022) Impact of quasi-biweekly oscillation on Southeast Asian cold surge rainfall monitored by TRMM satellite observation. Remote Sens 14:5200

Dong Z, Wang L, Gui S et al (2023) Diminished impact of the East Asian winter monsoon on the maritime continent rainfall after the late-1990s tied to weakened Siberian High-Aleutian low covariation. Clim Dyn. https://doi.org/10.1029/2022JD037336

Fu J, Liu M, Wang R et al (2022) Possible impact of boreal winter Siberian High on ENSO development in the following year. Front Earth Sci. https://doi.org/10.3389/feart.2022.885846

Gao W, Duan K, Li S (2021) A spatial–temporal analysis of cold surge days in northern China during 1960–2016. Nat Hazards 108:147–162

Gong D-Y, Ho C-H (2002) The Siberian High and climate change over middle to high latitude Asia. Theor Appl Climatol 72:1–9

Gong D-Y, Wang S-W, Zhu J-H (2001) East Asian winter monsoon and Arctic Oscillation. Geophys Res Lett 28:2073–2076

Hasanean HM, Almazroui M, Jones PD, Alamoudi AA (2013) Siberian High variability and its teleconnections with tropical circulations and surface air temperature over Saudi Arabia. Clim Dyn 41:2003–2018

He Z (2012) The synoptic causation analysis of a sandstorm over Henan province at the end of March 2006. Meteorol Mon 38:932–942 (**in Chinese**)

Holton JR, Hakim GJ (2013) An introduction to dynamic meteorology. Academic Press, Cambridge

Hu P, Chen W, Huang R et al (2019) Climatological characteristics of the synoptic changes accompanying South China Sea summer monsoon withdrawal. Int J Climatol 39:596–612

Hu P, Chen W, Wang L et al (2022) Revisiting the ENSO–monsoonal rainfall relationship: new insights based on an objective determination of the Asian summer monsoon duration. Environ Res Lett 17:104050

Huang R, Chen S, Chen W, Hu P (2018) Interannual variability of regional Hadley circulation intensity over Western Pacific during boreal winter and its climatic impact over Asia–Australia region. J Geophys Res Atmos 123:344–366

Iqbal MJ, Riaz SMF, Ghauri BMK (2013) Impact of Siberian High on rainfall variability over Northern part of Indo-Pak region. Arab J Geosci 6:3087–3092

Jeong J-H, Ou T, Linderholm HW et al (2011) Recent recovery of the Siberian High intensity. J Geophys Res Atmos 116:D23102

Jia XJ, Lin H, Yao X (2014) The influence of tropical pacific SST anomaly on surface air temperature in China. J Climate 27:1425–1444

Jia XJ, Wang S, Lin H, Bao Q (2015) A connection between the tropical Pacific Ocean and the winter climate in the Asian-Pacific region. J Geophys Res-Atmos 120:430–448

Keller LM, Morgan MC, Houghton DD, Lazear RA (2006) Synoptic–dynamic climatology of large-scale cyclones in the North Pacific. Mon Weather Rev 134:3567–3587

Kim E-S, Ahn J-B (2023) Study on the classification and characteristics of cold surge in South Korea. Int J Climatol 43:720–735

Kobayashi S, Ota Y, Harada Y et al (2015) The JRA-55 reanalysis: general specifications and basic characteristics. J Meteorol Soc Japan Ser II 93:5–48

Liebmann B, Marengo J (2001) Interannual variability of the rainy season and rainfall in the Brazilian Amazon Basin. J Clim 14:4308–4318

Liu B, Zhu C (2020) Diverse impacts of the Siberian High on surface air temperature in Northeast China during boreal winter. Int J Climatol 40:594–603

Lü Z, He S, Li F, Wang H (2019) Impacts of the autumn Arctic Sea ice on the intraseasonal reversal of the winter Siberian High. Adv Atmos Sci 36:173–188

Luo X, Wang B (2019) How autumn Eurasian snow anomalies affect East Asian winter monsoon: a numerical study. Clim Dyn 52:69–82

Ma T, Chen W, Graf H-F et al (2020) Different impacts of the East Asian winter monsoon on the surface air temperature in North America during ENSO and neutral ENSO years. J Clim 33:10671–10690

Ma T, Chen W, Chen S et al (2022) Different ENSO teleconnections over East Asia in early and late winter: role of precipitation anomalies in the tropical Indian Ocean and far Western Pacific. J Clim 35:4319–4335

Noska R, Misra V (2016) Characterizing the onset and demise of the Indian summer monsoon. Geophys Res Lett 43:4547–4554

Panagiotopoulos F, Shahgedanova M, Hannachi A, Stephenson DB (2005) Observed trends and teleconnections of the Siberian High: a recently declining center of action. J Clim 18:1411–1422

Pang B, Lu R (2019) Two distinct types of extratropical circulation anomalies associated with cold surges over the South China Sea. J Clim 32:5069–5084

Park HJ, Ahn JB (2016) Combined effect of the Arctic Oscillation and the Western Pacific pattern on East Asia winter temperature. Clim Dyn 46:3205–3221

Park S-B, Cho J-A, Park SS et al (2021) A possible linkage between dust frequency and the Siberian High in march over Northeast Asia. Atmosphere 12:176

Riaz SMF, Iqbal MJ (2017) Singular value decomposition analysis for examining the impact of Siberian High on winter precipitation variability over South Asia. Theor Appl Climatol 130:1189–1194

Shi N, Wang X, Tian P (2019) Interdecadal variations in persistent anomalous cold events over Asian mid-latitudes. Clim Dyn 52:3729–3739

Takaya K, Nakamura H (2005a) Geographical dependence of upper-level blocking formation associated with intraseasonal amplification of the Siberian High. J Atmos Sci 62:4441–4449

Takaya K, Nakamura H (2005b) Mechanisms of intraseasonal amplification of the cold Siberian High. J Atmos Sci 62:4423–4440

Takaya K, Nakamura H (2013) Interannual variability of the East Asian winter monsoon and related modulations of the planetary waves. J Clim 26:9445–9461

Tubi A, Dayan U (2013) The Siberian High: teleconnections, extremes and association with the Icelandic Low. Int J Climatol 33:1357–1366

Wang B (2006) The Asian monsoon. Springer-Verlag, Berlin Heidelberg New York

Wu MC, Chan JCL (1997) Upper-level features associated with winter monsoon surges over South China. Mon Weather Rev 125:317–340

Wu B, Ding S (2022) Cold-Eurasia contributes to arctic warm anomalies. Clim Dyn. https://doi.org/10.1007/s00382-022-06445-4

Wu B, Wang J (2002) Winter Arctic Oscillation, Siberian High and East Asian winter monsoon. Geophys Res Lett 29:1–4

Wu B, Su J, D'Arrigo R (2015) Patterns of Asian Winter climate variability and links to Arctic Sea ice. J Clim 28:6841–6858

Yanai M, Esbensen S, Chu J-H (1973) Determination of bulk properties of tropical cloud clusters from large-scale heat and moisture budgets. J Atmos Sci 30:611–627

Zhang R, Sumi A, Kimoto M (1996) Impact of El Niño on the East Asian Monsoon. J Meteorol Soc Japan Ser II 74:49–62

Zhang R, Zhang R, Zuo Z (2017) Impact of Eurasian spring snow decrement on East Asian summer precipitation. J Clim 30:3421–3437

Zhou W, Chan JCL, Chen W, Ling J, Pinto JG, Shao Y (2009) Synoptic-scale controls of persistent low temperature and icy weather over southern China in January 2008. Mon Weather Rev 137:3978–3991